chiometry resulted in the retention of both $-SiR_3$ and $-OMe$ groups in quantities high enough to stabilize nanometer-sized particles. Indeed, when the original precursor $\{Cd[P(SiMe_3)_2]_2\}_2$ was reexamined according to the altered stoichiometry of eq 3, soluble nanoclusters were also obtained.[16] We conclude that residual, covalent, surface-capping $-SiR_3$ and $-OMe$ substituents were responsible and necessary for arresting particle growth in the nanometer regime.

A separate route to Cd_3P_2 nanoclusters has been described by Henglein and co-workers.[17] In Henglein's procedure the precipitation of Cd_3P_2 from aqueous solutions of cadmium ions and PH_3 is arrested with the use of polymeric polyphosphate stabilizers, which presumably stabilize the particles by adhering to their surfaces. Henglein's and our results, as well as the work of others,[3e,f] indicate that the coordination chemistry of nanocluster surfaces is the critical issue in nanocluster stabilization. Our sol-gel-like synthesis, exemplified by eq 3, offers the ability to vary the covalent surface substituents, and offers many reaction variables to control the overall process. Further studies are in progress to establish the generality of the procedure, and to produce optimally stabilized, highly crystalline, monodispersed nanoclusters. We are also developing related procedures using precursors that are easier to obtain and to handle.

Acknowledgment. Support to W.E.B. was provided by the donors of the Petroleum Research Fund, administered by the American Chemical Society, the Monsanto Co., and an NSF Presidential Young Investigator award. Support to M.S.C. was provided by NSF DMR-9024502. Washington University provided equipment support. The Washington University High-Resolution NMR Service Facility was funded in part by NIH Biomedical Research-Support Shared-Instrument Grant 1 S10 RR02004 and a gift from the Monsanto Co. W.E.B. is grateful to Dr. Subhash C. Goel and Professor James K. Bashkin for many helpful discussions.

Supplementary Material Available: Figures showing digitized electron diffraction and X-ray diffraction patterns of bulk and nano-Cd_3P_2 (3 pages). Ordering information is given on any current masthead page.

(16) Goel, S. C.; Viano, A. M.; Adolphi, N. L.; Stoddard, R. D.; Conradi, M. S.; Gibbons, P. C.; Buhro, W. E. Unpublished.
(17) Haase, M.; Weller, H.; Henglein, A. *Ber. Bunsen-Ges. Phys. Chem.* **1988**, *92*, 1107.

Reviews

Zeolates: A Coordination Chemistry View of Metal-Ligand Bonding in Zeolite Guest-Host Inclusion Compounds

Geoffrey A. Ozin* and Saim Özkar†

Advanced Zeolite Materials Science Group, Lash Miller Chemical Laboratories, University of Toronto, 80 Saint George Street, Toronto, Ontario, Canada M5S 1A1

Received February 12, 1992

Various guests have been investigated in zeolite hosts in our laboratory over the past five years. From analysis of in situ spectroscopic observations (FT-IR, UV-vis, Mössbauer, DOR-MAS NMR) of the reaction sequences and structural features of precursors and products (EXAFS, Rietveld refinement of powder XRD data), the molecule size cavities and channels of zeolites respectively are viewed as providing macrospheroidal and macrocylindrical, multisite multidentate coordination environments toward encapsulated guests. By thinking, in particular, about the α- and β-cages of the zeolite Y host effectively as a "zeolate" ligand composed of interconnected and perfectly organized anionic aluminosilicate "crown ether-like" rings, the materials chemist is able better to understand and exploit the reactivity and coordination properties of the zeolite internal surface for the anchoring and self-assembly of a wide range of encapsulated guests (e.g., metal atoms, metal cations, metal clusters, coordination compounds, metal carbonyls, organometallics, metal oxides, and semiconductor nanoclusters. This approach helps with the design of synthetic strategies for creating novel guest-host inclusion compounds having possible applications in diverse areas of materials science, such as size/shape selective catalysis, nonlinear optics, quantum electronics, and photonics. To present this "crown ether-zeolate ligand analogy", we will focus attention on structurally well-defined examples of metal-zeolate bonding, involving mainly metal carbonyls and molecular metal oxides, housed within the diamond network of interlaced 13-Å supercages (α-cages) of zeolite Y, mainly taken from our recent work. A coordination chemistry view of metal-zeolate bonding in intrazeolite metal organic chemical vapor deposition type precursors and semiconductor nanocluster products is presented in a separate publication.[20]

Introduction

As a result of zeolite host-guest inclusion chemistry carried out in our laboratories over the past 5 years or so, it has become apparent that the molecule size cavities and channels of zeolites respectively behave as macrospheroidal and macrocylindrical, multisite multidentate ligands in their anchoring (complexing, coordinating, stabilizing) and structure directing properties toward a wide range of imbibed metal guests (e.g., metal atoms, metal cations, metal

† Chemistry Department, Middle East Technical University, 06531 Ankara, Turkey.

0897-4756/92/2804-0511$03.00/0

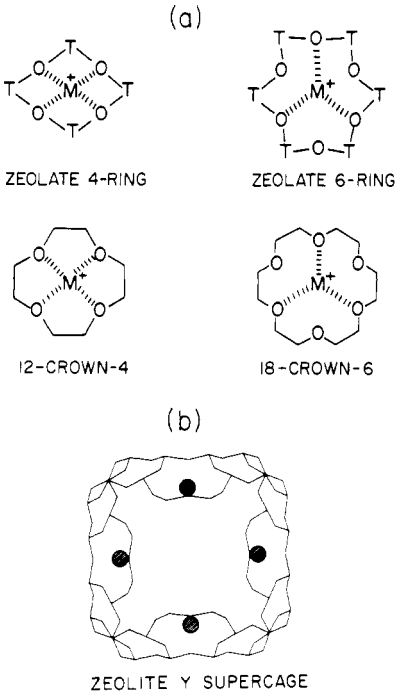

Figure 1. (a) Crown ether and zeolate ligand analogy. (b) Partial projection of the zeolite Y supercage showing four six-ring site II M^+ cations.

clusters, coordination compounds, organometallics, metal oxides and semiconductor nanoclusters). The interconnected and perfectly organized anionic aluminosilicate "crown-ether-like" rings, which constitute the inside lining (walls) of the void spaces in zeolites can be considered to function as a "zeolate" ligand from the perspective of coordination chemistry. This idea is illustrated in Figure 1. To present this crown ether–zeolate ligand analogy, we will focus attention on structurally well-defined examples of metal–zeolate binding within the diamond network of interlaced 13-Å supercages (α-cages) of zeolite Y, mainly taken from our recent work.

The Zeolate Ligand

On entering the nanometer dimension oxidic maze of α-cages in zeolite Y, one is confronted with two main types of binding site (Figure 1). These are best described as four-ring and six-ring "crown-ether-like" ligands constructed of tetrahedral SiO_4 and AlO_4 building units. Because of the much greater radius of the framework oxygens, relative to the Si^{4+} and Al^{3+} centers, the "curved" inside lining of the α-cage is dominated by the oxide sheath in which the Si^{4+} and Al^{3+} sites are effectively "buried" from view. For every Al^{3+} center, a framework negative charge is developed which is necessarily balanced by the incorporation of extraframework cations, usually Na^+, in the as-synthesized material, denoted $Na_{56}Y$ for Si/Al = 2.50. In zeolite Y, roughly 38 of these Na^+ cations reside in the eight α-cages of the cubic unit cell being distributed between two well-defined extraframework binding sites, denoted six-ring site II (32) and four-ring site III (6).[1] These cations interact mainly coulombically, with three and four nearest-neighbor oxygens of the six- and four-rings, respectively. They are positioned pyramidally above these sites (C_{3v} and C_{4v} site symmetries, respectively) protruding into the α-cage void space. They are "half-naked" and considered coordinately unsaturated. Gigantic electrostatic fields, estimated to be of the order of 10^6–10^8 V/cm are associated with these cationic "open coordination" sites.[2] These can have massive polarizing effects on encapsulated guests and play a key role in the coordination chemistry of the zeolate ligand. In this scheme of the α-cage, one therefore has cation-free and cation-bound four and six-ring coordination sites. Specifically one has a tetrahedral arrangement of four Na_{II}^+ (effectively an isotropic cation trap) coexisting on average with about one Na_{III}^+ in every α-cage.

The extraframework cations can be selectively ion exchanged for other M^{q+} cations (q = 1–3) or converted into Brønsted acid sites.[3] Hence the charge and spatial characteristics of these cationic centers and associated electric fields can be exquisitely fine tuned by judicious alterations of the identity, population and distribution of the charge-balancing cations (Lewis acid centers).[4] By thoughtful changes of the Si/Al ratio of the framework and choice of extraframework cations, one has a beautiful means of adjusting the electron density on the oxygen framework atoms (Lewis base centers).[4] From this point of view, the coordination chemist can begin to appreciate the aesthetic qualities of the zeolate ligand (Figure 1).

Metal Cation–Ligand Anchoring Interactions

Solvent-coordinated, crown-ether-complexed, polymer-anchored and oxide-bound metal cations (denoted $(S)M'^{q+}$) are well documented to interact with coordinated ligands in a wide variety of organometallic complexes.[5] A pervasive example in homogeneous and heterogeneous systems is the oxygen end of the carbonyl ligand and can be generalized in the following reaction scheme:

$$(S)M'^{q+} + L_nM(CO) \rightarrow (S)M'^{q+}\cdots(OC)ML_n$$

As a consequence of such metal cation–carbonyl interactions, one observes alterations in the structure, bonding, and reactivity of $L_nM(CO)$ compounds. The precise outcome of this kind of anchoring on the above properties depends on the Lewis acidity and degree of coordinative unsaturation of the metal cation site, as well as the Lewis basicity of the oxygen end of the interacting carbonyl ligand. In the following sections, we shall demonstrate that both cation-bound and cation-free four-ring and six-ring sites, that constitute the inside lining of the α-cage of zeolite Y, play a central role in the coordination chemistry of this zeolate ligand.

Site-Selective Anchoring of $M(CO)_6$ in $M'_{56}Y$

The saturation loading of $M(CO)_6$ (M=Cr, Mo, W) from the vapor phase into dehydrated $M_{56}'Y$ (M' = H, Li, Na, K, Rb, Cs) amounts of $16M(CO)_6$/unit cell or $2M(CO)_6$/α-cage.[6] EXAFS structure analysis of $8\{M(CO)_6\}$–$M'_{56}Y$ (M = Mo, W; M' = Na, Rb) using the Mo K-edge, W LIII-edge, and Rb K-edge,[6,7] demonstrates that the integrity of the hexacarbonylmetal(0) guest is maintained intact on encapsulation in zeolite Y, with only minor perturbations of the M–*C*–O and M–C–*O* bond lengths

(1) Fitch, A. M.; Jobic, H.; Renouprez, A. *J. Phys. Chem.* **1986**, *90*, 1311.

(2) Preuss, E.; Linden, G.; Peuckert, M. *J. Phys. Chem.* **1985**, *89*, 2955. Yamazaki, T.; Watanuki, I.; Ozawa, S.; Ogino, Y. *Langmuir* **1988**, *4*, 433.

(3) Dwyer, J.; Dyer, A. *Chem. Ind.* **1984**, 237 and references therein.

(4) Mortier, W. J.; Schoonheydt, R. A. *Prog. Solid State Chem.* **1985**, *16*, 1 and references therein.

(5) (a) Darensbourg, M. Y.; Jimenez, P.; Sackett, J. R.; Hanckel, J. M.; Kump, R. L. *J. Am. Chem. Soc.* **1982**, *104*, 1521. Rhodes, L. F.; Huffman, J. C.; Caulton, K. G. *J. Am. Chem. Soc.* **1985**, *107*, 1759. Chaudret, B.; Commenges, G.; Jalon, F.; Otero, A. *J. Chem. Soc., Chem. Commun.* **1989**, 210. (b) Roy, P. S.; Weighardt, K. *Inorg. Chem.* **1987**, *26*, 1885.

(6) Özkar, S.; Ozin, G. A.; Moller, K.; Bein, T. *J. Am. Chem. Soc.* **1990**, *112*, 9575.

(7) Moller, K.; Bein, T.; Özkar, S. Ozin, G. A. *J. Phys. Chem.* **1991**, *95*, 5276.

Table I. EXAFS Structure Analysis Results for $Rb_{56}Y$, $8\{Mo(CO)_6\}$–$Rb_{56}Y$, $8\{Mo(CO)_3\}$–$Rb_{56}Y$, $8\{Mo\}$–$Rb_{56}Y$, and $8\{Mo_2\}$–$Na_{56}Y$[6,11,12]

sample	bond length, Å	coordination no.	static disorder, Å²	inner potential, eV
$Rb_{56}Y$				
ZO(Rb)	2.75	2.6	0.0000	9.4
$8\{Mo(CO)_6\}$–$Rb_{56}Y$				
ZO(Rb)*OC*Mo	2.77	2.8	0.0030	8.8
ZORb*OC*(Mo)	2.06	6.0	−0.0012	0.5
ZoRb*OC*(Mo)	3.21	8.0	0.0028	−0.9
$8\{Mo(CO)_3\}$–$Rb_{56}Y$				
ZO(Rb)*OC*Mo	2.76	2.7	0.0000	7.4
ZO(Mo)*CO*	1.93	3.4		
ZO(Mo)*CO*	3.06	3.4	0.0017	−0.2
ZO(Mo)CO	1.82	2.0		
$8\{Mo\}$–$Rb_{56}Y$				
ZO(Rb)	2.76	1.8	−0.0030	6.8
ZO(Mo)	2.08	0.6	−0.0040	−4.5
$8\{Mo_2\}$–$Na_{56}Y$				
ZO(Mo)Mo	2.1	1.8		
ZO(Mo)*Mo*	2.8	1.0		

[a] Element-specific X-ray edge is indicated in parentheses; bond length and coordination with respect to italicized element.

(Table I). Small changes in the oxygen coordination number around the Rb^+ cations indicate ZORb^+···OC anchoring interactions. However, as only 16 site II Rb^+ cations out of a total of 56 can probably participate in this scheme, this result is considered equivocal. The mid-IR spectra of the entrapped $M(CO)_6$ guest, display fully resolved ν(CO) sextets indicative of an α-cage anchoring site with a symmetry of C_{2v} or lower.[6] Together with the cation ionic potential dependence of these ν(CO) frequencies, one deduces that the $M(CO)_6$ guest is anchored via *trans*-carbonyls most likely to two site II cations, that is

$$trans\text{-}(ZOM'_{II})\cdots(OC)M(CO)_4(CO)\cdots(M'_{II}OZ)$$

Convincing support in favor of this anchoring scheme is obtained by a combination of site-selective mid-IR, far-IR, and DOR-MAS NMR spectroscopies.[8,9] For example, by monitoring adsorption-induced perturbations in the mid-IR $\nu(OH_\alpha)$ modes and far-IR Na^+ translatory modes on adsorbing $M(CO)_6$ into $Na_{40}H_{16}Y$ (the latter containing on average two α-cage Brønsted acid sites and two site II Na^+ cations), one determines that for a half-loaded sample $8\{M(CO)_6\}$–$Na_{40}H_{16}Y$, the $M(CO)_6$ guest is homogeneously distributed amongst the available α-cages, binding specifically to the two site II Na^+ cations. The Brønsted acid sites remain untouched. In the fully loaded sample $16\{M(CO)_6\}$–$Na_{40}H_{16}Y$, containing $2M(CO)_6/\alpha$-cage, the two site II Na^+ cations as well as the two Brønsted acid sites are tied up in anchoring interactions. The results of this study are summarized in Figure 2. Site-selective ^{23}Na MAS NMR and DOR NMR studies of $M(CO)_6$ in $Na_{56}Y$ and $Na_{40}H_{16}Y$ provide convincing support for the proposed anchoring scheme. For example, Figure 3 shows the ^{23}Na DOR NMR spectra of $n\{Mo(CO)_6\}$–$Na_{56}Y$ (n = 0, 4, 8, 16). The loading dependence is apparent in the NMR spectra as a substantial enhancement of the intensity of the ^{23}Na resonance at around −25 ppm. This peak is therefore ascribed to the anchoring Na^+ in site II within the α-cage, an assignment independently confirmed by a ^{23}Na DOR study of cation exchange in zeolite Y.[8] The intensity of the signals at −5 ppm and −41 ppm, ascribed to site I and I′, respectively,[8] do not seem to be much affected by the $Mo(CO)_6$ adsorption. From inspection of Figure 3, one essentially "discovers" the site II Na^+ signal through its selective anchoring to $Mo(CO)_6$ moieties.[8] The transformation of "half-naked" ZONa^+ into coordinated ZONa^+···OC increases the symmetry around the site II Na^+

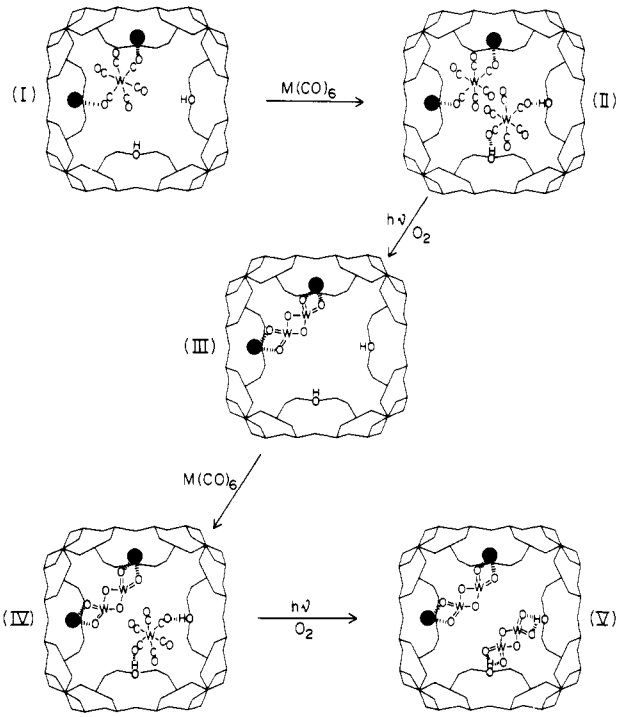

Figure 2. Site selective anchoring of $W(CO)_6$ and W_2O_6 in $Na_{40}H_{16}Y$.[9]

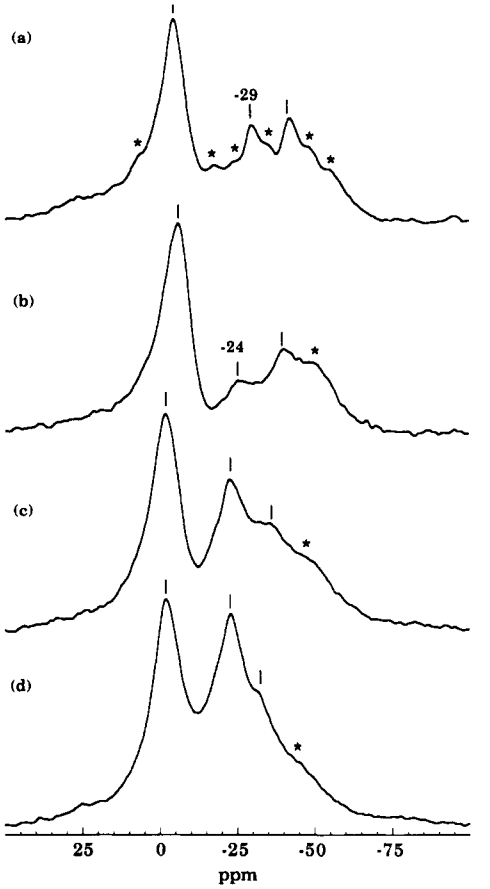

Figure 3. ^{23}Na DOR NMR spectra of $n\{Mo(CO)_6\}$–$Na_{56}Y$, where n = 0 (a), 4 (b), 8 (c), 16 (d).[8]

(8) Jelinek, R.; Ozin, G. A.; Özkar, S. *J. Phys. Chem.*; *J. Am. Chem. Soc.*, in press.
(9) Ozin, G. A.; Özkar, S.; Macdonald, P. *J. Phys. Chem.* **1990**, *94*, 6939.

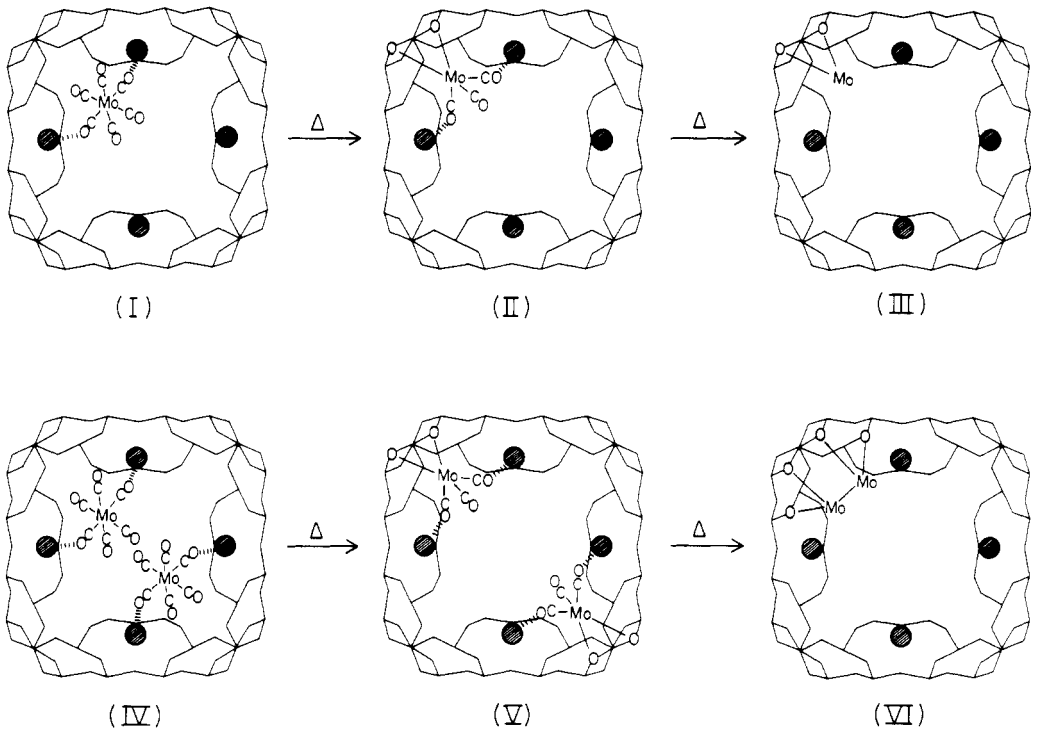

Figure 4. Controlled vacuum thermal decarbonylation of $8\{Mo(CO)_6\}$–$Na_{56}Y$ yields intermediate $8\{Mo(CO_3)\}$–$Na_{56}Y$ and final product $8\{Mo\}$–$Na_{56}Y$, the latter containing zeolate stabilized molybdenum atoms (ZO)Mo, while $16\{Mo(CO)_6\}$–$Na_{56}Y$ leads to the final product $8\{Mo_2\}$–$Na_{56}Y$ containing zeolate-stabilized molybdenum dimers $(ZO)_2\cdots Mo_2\cdots(OZ)_2$.[6,12,13]

nucleus and/or reduces the Na^+ motion within the α-cage to the extent that "missing" ^{23}Na intensity is recovered. Thus, the sharp signal ascribed to the site II Na^+ increases progressively as more $Mo(CO)_6$ guest is adsorbed into the α-cage of zeolite Y as shown in Figure 3b–d.[8] Interestingly, the shielding of site II Na^+ decreases with increasing loading of $Mo(CO)_6$ in $Na_{56}Y$, which alerts one to negative cooperative deanchoring effects involving $ZONa^+\cdots OC$ interactions. This important phenomenon is described more fully later on in the context of intrazeolate kinetics.[18]

Summarizing up to this point, one can state that the tetrahedral "ion-trap" built up of four site II Na^+ cations selectively captures up to $2M(CO)_6/\alpha$-cage. These are each anchored by *trans*-carbonyl ligands in two site II Na^+ cations. They are organized orthogonally along opposite edges of the tetrahedron of four site II Na^+ cations. The actual distribution of $M(CO)_6$ guests amongst the α-cages of $Na_{56}Y$, below saturation loading, is a fascinating problem which can be very effectively probed by loading-, temperature-, and pressure-dependent ^{129}Xe NMR spectroscopy. Dynamical effects involving the $M(CO)_6$ guest at the Na_{II}^+ anchoring sites in the α-cage of $Na_{56}Y$ are conveniently probed by loading- and temperature-dependent ^{13}C MAS NMR spectroscopy. Studies of this type are currently underway in our laboratories.

Vacuum Thermal "Partial" Decarbonylation of $n\{M(CO)_6\}$–$M'_{56}Y$

A controlled vacuum thermal treatment of samples $n\{M(CO)_6\}$–$M'_{56}Y$ for M = Cr, Mo, W and M′ = Li, Na, K, Rb, Cs provides a mild, clean decarbonylation route to yield the corresponding $n\{M(CO)_3\}$–$M'_{56}Y$ species, with little evidence for appreciable concentrations of reactive intermediates $n\{M(CO)_m\}$–$M'_{56}Y$, where m = 5, 4.[6] The mid-IR ν(CO) spectral patterns are diagnostic of a C_{3v} pyramidal geometry for the $M(CO)_3$ moiety in $n\{M(CO)_3\}$–$M'_{56}Y$, only for 2 of the 15 possibilities, namely, M = Mo, W and M′ = Cs. The remaining 13 cases exhibit a C_s distorted pyramidal shape for the $M(CO)_3$ fragment. These conclusions are convincingly confirmed by the observed and calculated ν(CO) mid-IR isotopic frequency and intensity spectral patterns for $n\{M(^{12}CO)_x(^{13}CO)_{3-x}\}$–$M'_{56}Y$, where x = 0–3 for two representative cases, namely, M = W, M′ = Li (C_s) and M = W, M′ = Cs (C_{3v}).[10]

The cation dependence of the ν(CO) frequencies for $n\{M(CO)_3\}$–$M'_{56}Y$ is quite different from that observed for $n\{M(CO)_6\}$–$M'_{56}Y$, immediately signalling the possibility of a primary oxygen framework anchoring location for the $M(CO)_3$ moiety rather than cation stabilization as found for $M(CO)_6$. One observes only a "minor" $\Delta\nu_{CO}$ effect following the trend $Li^+ < Na^+ < K^+ < Rb^+ < Cs^+$ for the former but a "major" $Li^+ > Na^+ > K^+ > Rb^+ > Cs^+$ effect for the later. In the case of $M(CO)_3$ this can be rationalized in terms of the Sanderson electronegativity of the zeolate ligand,[4] which is a useful measure of the electron density (Lewis basicity) of the oxygen framework atoms. Hence the highest ionic potential cation Li^+ provides the lowest basicity zeolate ligand in $Li_{56}Y$, while the opposite is true for $Cs_{56}Y$. The result of this is that the most strongly lattice stabilized $M(CO)_3$ moiety is to be found in $Cs_{56}Y$ which as a result has the lowest frequency mild-IR ν(CO) modes. This zeolate Lewis basicity effect appears to be counterbalanced somewhat by secondary $ZOM'\cdots OC$ interactions of the kind illustrated in Figure 4, which would be expected to be most pronounced for M′ = Li. In this way one can rationalize the cation dependence of the ν(CO) modes of $n\{M(CO)_3\}$–$M'_{56}Y$ as well as their correlation with the respective XPS O(1s) and Mo(3d) energies.[11] Here one finds that the most basic zeolate ligand in $Cs_{56}Y$ yields the lowest O(1s) energies, which through $O(2p\pi) \rightarrow Mo(3d\pi) \rightarrow CO(2p\pi^*)$ charge transfers creates the lowest Mo(3d) energies and lowest ν(CO) frequencies. An EXAFS

(10) Ozin, G. A.; Özkar, S.; McIntosh, D. *J. Chem. Soc., Chem. Commun.* **1990**, 841.
(11) Okamoto, Y.; Imanaka, T.; Asakura, K.; Iwasawa, Y. *J. Phys. Chem.* **1991**, *95*, 3700.
(12) Yong, Y. S.; Howe, R. F.; Hughes, A. E.; Jaeger, H.; Sexton, B. A. *J. Phys. Chem.* **1987**, *91*, 6331.

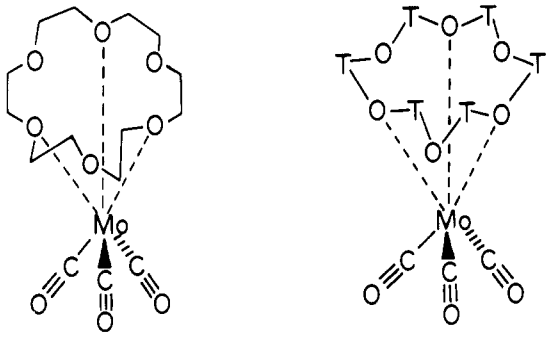

(I) (II)

Figure 5. 18-Crown-6 analogue of zeolate stabilized *fac*-tricarbonylmolybdenum(0).[14]

structure analysis for $8\{Mo(CO)_3\}$–$Rb_{56}Y$[6] was the first to provide strong support for these proposals concerning lattice-anchored $M(CO)_3$. The best fit carbonyl and oxygen coordination numbers yield the stoichiometry $(ZO)_{2,3}$···$Mo(CO)_3$ with a dramatic decrease in the Mo–*C*–O and Mo–C–*O* bond lengths compared to those found in the parent $8\{Mo(CO)_6\}$–$Rb_{56}Y$ (Table I). In a subsequent EXAFS study[11] it was shown that the Mo–*C*–O and Mo–*O*–Z bond lengths are found to parallel the Lewis basicity of the zeolate ligand, that is, shortening on passing from $Li_{56}Y$ to $Cs_{56}Y$ and on decreasing the Si/Al ratio.

The above multiprong characterization of $n\{M(CO)_3\}$–$M'_{56}Y$ provides an aesthetically pleasing picture of a zeolate-stabilized $M(CO)_3$ moiety, which when taken in combination with the existence and properties of the known materials (18-crown-6)$M(CO)_3$, strikingly brings forth the analogy between crown ether and zeolate ligand binding to the $M(CO)_3$ moiety as illustrated in Figure 5.

Intrazeolite chemical reactions[6] of $n\{M(CO)_3\}$–$M'_{56}Y$ with C_6H_6, C_7H_8, and PMe_3 yield products which also reenforce the view of zeolate-stabilized $(ZO)_{2,3}$···$M(CO)_3$ moieties. The products are $n\{(\eta^6\text{-}C_6H_6)M(CO)_3\}$–$M'_{56}Y$, $n\{(\eta^6\text{-}C_7H_8)M(CO)_3\}$–$M'_{56}Y$, and $n\{M(CO)_3(PMe_3)_m\}$–$M'_{56}Y$ (m = 1–3), respectively. Early results indicate that the reactivity of the $(ZO)_{2,3}$···$M(CO)_3$ moieties with respect to this kind of "zeolate ligand substitution" reaction parallels the Lewis basicity of the zeolate ligand. Quantitative intrazeolate kinetic measurements will be needed to substantiate this fascinating idea (see later).

Vacuum Thermal "Complete" Decarbonylation of $n\{Mo(CO)_6\}$–$M'_{56}Y$

If one continues the decarbonylation of $n\{Mo(CO)_6\}$–$M'_{56}Y$ in a "controlled" manner beyond the $n\{Mo(CO)_3\}$–$M'_{56}Y$ stage, one can detach all carbonyl ligands to yield $n\{Mo\}$–$M'_{56}Y$ samples. Two recent EXAFS studies[6,13] of these "completely" decarbonylated products (Table I) show that $8\{Mo(CO)_6\}$–$Rb_{56}Y$ containing a single $Mo(CO)_6$ guest/α-cage yields oxygen-framework-stabilized "atomic" molybdenum, found to be (ZO)···Mo with R(Mo–O) = 2.08 Å and $N_{MoO} \cong 0.6$ illustrated in Figure 4. Amazingly, fully loaded $16\{Mo(CO)_6\}$–$Na_{56}Y$, with two $Mo(CO)_6$ guests/α-cage, produces oxygen-framework-stabilized "diatomic" molybdenum, shown to be $(ZO)_2$···Mo_2···$(OZ)_2$ with R(Mo–O) = 2.1 Å, R(Mo–Mo) = 2.8 Å, $N_{MoO} \cong 1.8$, $N_{MoMo} \cong 1$, also illustrated in Figure 4. These results force one to the inescapable conclusion that a single α-cage zeolate stabilized $(ZO)_{2,3}$···$Mo(CO)_3$ moiety strips off its three carbonyl ligands to yield a zeolate-stabilized Mo atom (ZO)···Mo, whereas two α-cage-zeolate-stabilized $(ZO)_{2,3}$···$Mo(CO)_3$ moieties, on each stripping off their three carbonyls, unite in the "same" α-cage to produce a zeolate-stabilized Mo_2 dimer, $(ZO)_2$···Mo_2···$(OZ)_2$ (Figure 4).

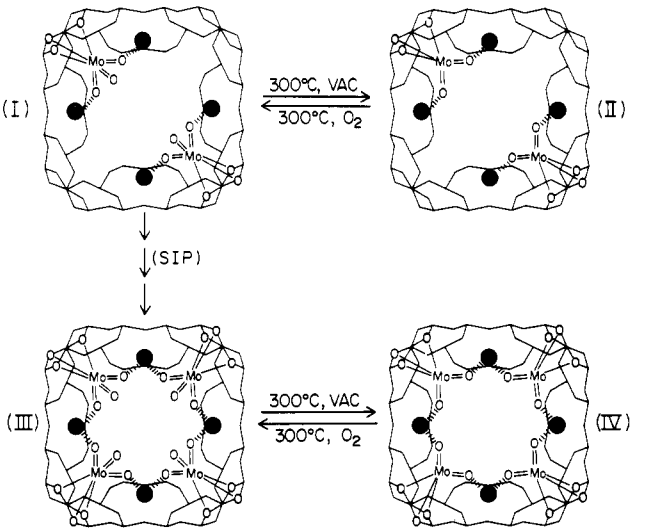

Figure 6. Redox interconvertible $n\{MoO_{3-x}\}$–$Na_{56}Y$, where $0 < n \leq 32$ and $x = 0, 1$.[14] (Note that I and II are the favored "isomers" from ^{23}Na DOR NMR studies[8]).

Redox Interconvertible "Molecular" Molybdenum and Tungsten Oxides in Sodium Zeolite Y

Photooxidation Products. It is well-known that despite the chemical similarity of molybdenum and tungsten, there exist differences between them in compounds of disparate types which are often surprising and sometimes difficult to explain. The photooxidation of hexacarbonylmolybdenum(0)[14] and hexacarbonyltungsten(0)[15,16] with gaseous dioxygen in sodium zeolite Y turns out to be a case in point and definitely falls into this unexpected category. Let us examine highlights of these two systems. The photooxidation process is clean and quantitative and is described by the reaction stoichiometry

$$n\{M(CO)_6\}\text{–}Na_{56}Y + 9/2nO_2 \xrightarrow{h\nu} n\{MO_3\}\text{–}Na_{56}Y + 6nCO_2$$

in a single impregnation/photooxidation step. This transformation can be conducted over the full loading range $0 < n \leq 16$ where $16\{M(CO)_6\}$–$Na_{56}Y$ represents saturation adsorption, corresponding to $2\{M(CO)_6\}/\alpha$-cage.

A multiprong analysis (PXRD, EXAFS, MAS/DOR-NMR, EPR, XPS, UV-vis, FTIR, RAMAN, TEM, STEM-EDX, gravimetry) has been used to structurally define the precursors and photooxidation products in these two systems. The former have been described earlier in this paper as *trans*-$(ZONa_{II})$···$(OC)M(CO)_4(CO)$···$(Na_{II}OZ)$ for both M = Mo, W (Figure 2). Over the entire loading range $0 < n \leq 16$ the metal (VI) oxide photoproducts are located in the α-cage of $Na_{56}Y$. The product in the case of molybdenum contains oxygen-framework- and Na^+-cation-stabilized MoO_3 monomers, denoted (ZO)···MoO_3···(NaOZ), where ZO represents an oxygen framework six-ring or four-ring "primary" anchoring interaction and NaOZ represents a site II or site III Na^+ cation "secondary"

(13) Coddington, J. H.; Howe, R. F.; Yong, Y. S.; Asakara, K.; Iwasawa, Y. *J. Chem. Soc., Faraday Trans.* **1990**, *86*, 1015.

(14) Özkar, S.; Ozin, G. A.; Prokopowicz, R. *J. Am. Chem. Soc.*, submitted.

(15) Ozin, G. A.; Özkar, S. *J. Phys. Chem.* **1990**, *94*, 7556.

(16) Ozin, G. A.; Özkar, S.; Prokopowicz, R. *J. Am. Chem. Soc.*, submitted.

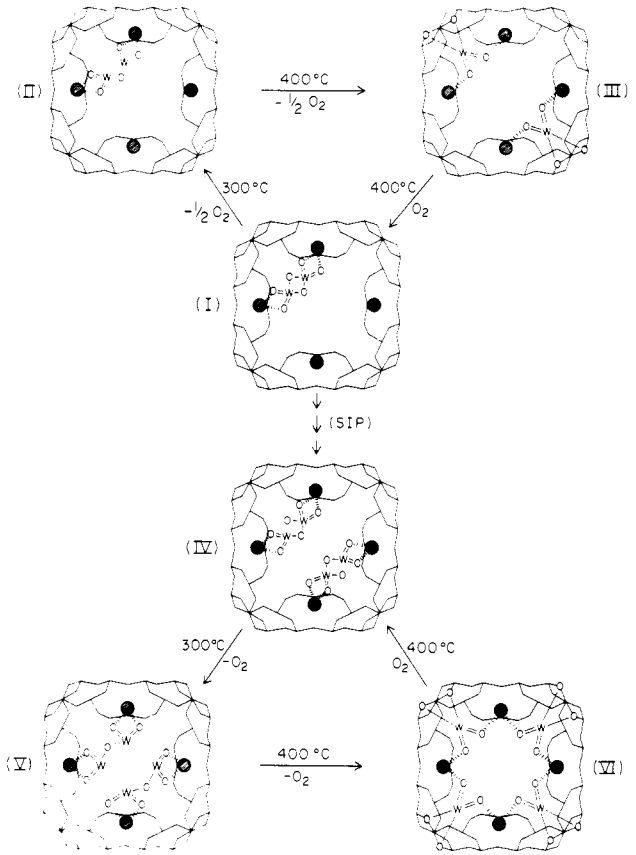

Figure 7. Redox interconvertible $n\{WO_{3-x}\}$–$Na_{56}Y$, where $0 < n \leq 32$ and $x = 0, 0.5, 1$.[16] (Note that III is the favored "isomer" from ^{23}Na DOR NMR studies[8]).

interaction (the latter involving the oxygen atom of an oxomolybdenum(VI) bond). In the case of tungsten, the phooxidation products is $(ZONa_{II})\cdots O_2W(\mu\text{-}O)_2WO_2\cdots(Na_{II}OZ)$ where the W_2O_6 dimer is tethered by sodium cation–dioxotungsten(VI) group linkages. These structural conclusions, arrived at using the powerful group of physicochemical characterization methods mentioned above, are illustrated in Figure 6 and 7. The EXAFS results are summarized in Table II.

From consideration of the steric and spatial demands of $M(CO)_6$ relative to MoO_3 monomer and W_2O_6 dimer, it can be determined that the process of photooxidizing precursor to product within the α-cage "creates space" (Figures 2, 6, and 7), thereby allowing sequential impregnation/photooxidation steps (denoted SIP) to be achieved. In the special circumstances of repetitive saturation–adsorption followed by photooxidation, one can approach a maximally loaded photoproduct composition of $32\{MO_3\}$–$Na_{56}Y$ as illustrated in the following scheme:

$$16M(CO)_6\text{–}Na_{56}Y \rightarrow 16MO_3\text{–}Na_{56}Y$$

$$8M(CO)_6,\ 16MO_3\text{–}Na_{56}Y \rightarrow 24MO_3\text{–}Na_{56}Y$$

$$4M(CO)_6,\ 24MO_3\text{–}Na_{56}Y \rightarrow 28MO_3\text{–}Na_{56}Y$$

$$\vdots$$

$$1M(CO)_6,\ 31MO_3\text{–}Na_{56}Y \xrightarrow{SIP} 32MO_3\text{–}Na_{56}Y$$

A combination of spectroscopy, diffraction, and microscopy has demonstrated that the MoO_3 monomer and W_2O_6 structures are maintained across the full loading range $0 < n \leq 32$. The half-loaded samples $n = 16$ are described as a supralattice of monomers $16\{MoO_3\}$–$Na_{56}Y$ and dimers $8\{W_2O_6\}$–$Na_{56}Y$ (Figures 6 and 7), whereas the completely filled samples $n = 32$ comprise a supralattice

Table II. EXAFS Structure Analysis Results for $n\{MO_{3-x}\}$–$Na_{56}Y$, Where M = Mo, W; $0 < n \leq 32$, $0 \leq x \leq 1$[7,14,16]

sample	bond length, Å	coordination no.	static disorder, Å²	inner potential, eV
$16\{MoO_3\}$–$Na_{56}Y$				
Z*O*(Mo)O	1.73	3.2	0.0000	1.5
ZO(Mo)*O*	1.88	2.8	0.0019	1.6
$16\{MoO_2\}$–$Na_{56}Y$				
Z*O*(Mo)*O*	1.80	5.0	0.0024	0.6
$16\{WO_3\}$–$Na_{56}Y$				
ZONa*O*(W)OW	1.77	2.2	0.0008	3.8
ZONaO(W)*O*W	1.94	1.8	−0.0009	3.8
ZONaO(W)O*W*	3.30	1.3	0.0009	−6.9
$28\{WO_3\}$–$Na_{56}Y$				
ZONa*O*(W)OW	1.75	2.2	0.0030	3.6
ZONaO(W)*O*W	1.95	2.2	0.0010	−3.9
ZoNaO(W)O*W*	3.24	1.4	0.0016	4.3
$32\{WO_3\}$–$Na_{56}Y$				
ZONa*O*(W)OW	1.78	1.7	−0.0004	4.1
ZONaO(W)*O*W	1.96	1.9	0.0008	2.4
ZONaO(W)O*W*	3.31	1.4	0.0009	−10.0
$16\{WO_{2.5}\}$–$Na_{56}Y$				
ZONa*O*(W)OW	1.77	2.1	0.0009	6.1
ZONaO(W)*O*W	1.94	1.1	−0.0011	2.8
ZONaO(WO)O*W*	3.30	1.3	0.0028	−10.0
$32\{WO_{2.5}\}$–$Na_{56}Y$				
ZONa*O*(W)OW	1.83	2.2	0.0045	5.0
ZONaO(W)*O*W	2.00	0.8	−0.0034	−4.3
ZONaO(W)O*W*	3.30	2.9	0.0028	−10.0
$16\{WO_2\}$–$Na_{56}Y$				
ZONa*O*(W)*O*	1.81	4.1	0.0028	0.4
$32\{WO_2\}$–$Na_{56}Y$				
ZONa*O*(W)*O*	1.84	4.0	0.0040	1.9

[a] Element-specific X-ray edge is indicated in parentheses; bond lengths and coordination number with respect to italicized element.

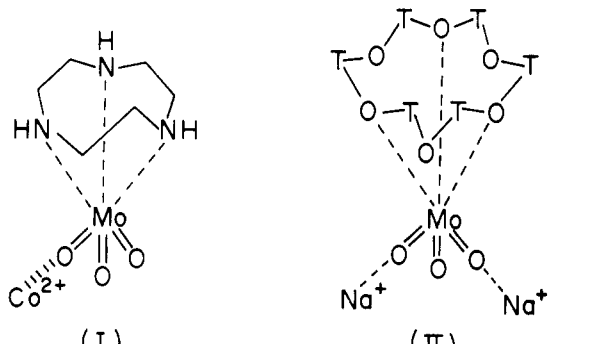

Figure 8. 1,4,7-Triazononane analogue of zeolate-stabilized *fac*-tricarbonylmolybdenum(0) with the oxomolybdenum(VI) groups of *fac*-$LMoO_3$ acting as Lewis bases toward cationic metal centers.[14]

of monomers $32\{MoO_3\}$–$Na_{56}Y$ and dimers-of-dimers $16\{(W_2O_6)_2\}$–$Na_{56}Y$ (Figures 6 and 7). CHEM-X molecular graphics representations of the latter show that the two dimers jointly occupying each α-cage, are configured orthogonally with respect to each other, anchored at opposite edges of the tetrahedral array of $4Na_{II}^+$ cations (a kind of "ion trap", Figure 7). Similarly, the former are best described as a tetrahedral array of monomeric *fac*-MoO_3 moieties (with three shorter Mo=O bonds) stabilized through coordination to three framework oxygen atoms (longer Mo—O bonds) of a four-ring or six-ring lattice site (Figure 6). The "zeolate" ligating properties to this monomeric *fac*-trioxomolybdenum(VI) unit (II, Figure 8) find remarkable molecular analogues in $LMoO_3$ complexes (I, Figure 8), where L represents, for example, 1,4,7-triazocyclononane.[5b] The latter is formed essentially quantita-

tively by the oxidative decarbonylation of $LMo(CO)_3$ by 30% H_2O_2 in THF at 45 °C.

As mentioned earlier for $n\{Mo(CO)_6\}$–$Na_{56}Y$, ^{23}Na MAS and DOR NMR spectra clearly depict site II Na^+ cation adsorption-induced chemical shifts and intensity alterations (Figure 3). Observations of this kind demonstrate the presence of Na^+ cation based anchoring interactions. Similar effects are observed for the site II Na^+ cations in the photooxidation products $n\{MO_3\}$–$Na_{56}Y$. This strongly suggests that the oxygen atom of at least one of the terminal oxometal(VI) groups in the monomeric *fac*-trioxomolybdenum(VI) MoO_3 moiety and dimeric tetraoxodi-μ-oxoditungsten(VI) W_2O_6 moiety may bind to a site II Na^+ cation. This idea is illustrated in Figures 6 and 7.

In the case of, for example, (ZO)···MoO_3···(NaOZ), this proposal is beautifully supported by comparison with the ligating properties of the MoO_3 moiety in $LMoO_3$ complexes toward transition metal cationic centers such as Fe^{2+}, Co^{2+}, and Ni^{2+}.[5b] For instance, the reaction of $LMoO_3$ with $Co(ClO_4)_2 \cdot 6H_2O$ in dry methanol yields a blue solution from which crystals of composition $[(LMoO_3)_4Co](ClO_4)_2$ precipitate, whereas the same reaction carried out in aqueous solution produces a pink solution containing $[Co(H_2O)_6]^{2+}$. This indicates that the oxygen atoms of the oxomolybdenum(VI) bonds in $LMoO_3$ units are weaker donors than water but stronger than methanol. It is believed that the central Co(II) ion is tetrahedrally surrounded by four oxygen atoms, one from each $LMoO_3$ unit, which function as monodentate neutral ligands (I, Figure 8).

The analogy between (ZO)···MoO_3···(Na^+OZ) and (L)···MoO_3···(Co^{2+}) therefore becomes clear, bringing forth again, in a most vivid way, the idea of the zeolite cavity acting as a macrospheroidal multidentate multisite zeolate ligand toward various guests, in this particular case a *fac*-trioxomolybdenum(VI) unit (Figure 8).

Thermal Vacuum Reduction Products. An especially fascinating and potentially useful property of these MoO_3 monomers and W_2O_6 dimers is their intrazeolite redox chemistry. Vacuum thermal treatment results in a clean reductive elimination of O_2 in what appears to be *two* distinct steps, around 300 and 400 °C for W_2O_6 and *one* distinct step around 300 °C for MoO_3 according to the respective reaction stoichiometries

$$n\{WO_3\}\text{–}Na_{56}Y \xrightarrow{300\ ^\circ C} n\{WO_{2.5}\}\text{–}Na_{56}Y \xrightarrow{400\ ^\circ C} n\{WO_2\}\text{–}Na_{56}Y$$

$$n\{WO_2\}\text{–}Na_{56}Y \xrightarrow[O_2]{300\ ^\circ C} n\{WO_3\}\text{–}Na_{56}Y$$

$$n\{MoO_3\}\text{–}Na_{56}Y \underset{300\ ^\circ C,\ O_2}{\overset{300\ ^\circ C,\ \text{vacuum}}{\rightleftharpoons}} n\{MoO_2\}\text{–}Na_{56}Y$$

With increasing loading $0 < n \leq 32$, the $n\{WO_3\}$–$Na_{56}Y$ parent compound changes colour from white to light gray, the $n\{WO_{2.5}\}$–$Na_{56}Y$ intermediate phase changes from metallic blue to metallic gray, and the $n\{WO_2\}$–$Na_{56}Y$ final phase produced changes from white to light gray. The latter material can be cleanly and quantitatively reoxidized at 300 °C in O_2 back to the starting material, but without any evidence of passing through the intermediate phase as shown above. Vacuum thermal treatment of $n\{MoO_3\}$–$Na_{56}Y$ at 300 °C cleanly transforms the white photooxidation product to puce-colored samples of $n\{MoO_2\}$–$Na_{56}Y$ over the entire loading range $0 < n \leq 32$. This reduction process can be quantitatively reversed by exposing the sample to O_2 at 300 °C.

A multiprong analysis, similar to that employed to study the photooxidation products described above, was applied to the intermediate and final reduction product phases in these systems (Table II). This investigation has served to elucidate certain key aspects relating to their structure, bonding, and electronic properties. Briefly summarizing key features of these results, one finds in the tungsten oxide system at $n = 16$, the intermediate phase contains a supralattice of μ-oxo-bridged dimers (ZONa_{II})···$O_2W(\mu\text{-}O)WO_2$···(Na_{II}OZ), while the final phase contains a supralattice of monomers (ZO)···WO_2···(Na_{II}OZ) with the structures illustrated in Figure 7. At $n = 32$, the intermediate phase is comprised of a supralattice of tetramers (ZONa_{II})···$O_4W_2(\mu\text{-}O)_2W_2O_4$···($Na_{II}$OZ), while the final product retains a supralattice of monomers (ZO)···WO_2···(Na_{II}OZ), with the structures depicted in Figure 7. All of these phases appear to be diamagnetic, spin-paired (EPR silent, NMR active) materials. It is clear from XPS that $n\{WO_2\}$–$Na_{56}Y$ unequivocally contains W^{4+}. The XPS data for $n\{WO_{2.5}\}$–$Na_{56}Y$ favor an assignment containing superexchange coupled W^{5+}···W^{5+} centers in the W_2O_5 dimer ($n = 16$) with exchange-coupled W_2O_5 "dimer pairs" in the W_4O_{10} tetramer ($n = 32$), rather than having to invoke mixed-valence W^{4+}···W^{6+} sites (Figure 7).

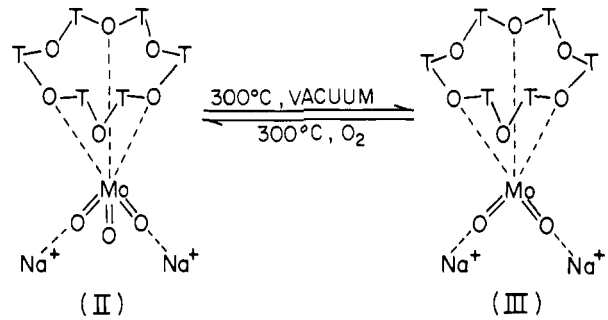

Figure 9. "Primary" anchoring oxygen framework sites and "secondary" anchoring extraframework Na^+ cations in (ZO)···MoO_3···(Na_{II}OZ) and (ZO)···MoO_2···(Na_{II}OZ) redox-interconvertible pairs.[14]

Compared to the tungsten oxide system, the molybdenum oxide story is rather straightforward. The sole reduction product over the entire loading range $0 < n \leq 32$ is the (ZO)···MoO_2···(Na_{II}OZ) monomer, containing a "primary" oxygen framework anchoring interaction via those oxygens of a six-ring or four-ring site to a monomeric *cis*-MoO_2 moiety, with "secondary" anchoring interactions which involve at least one of the oxomolybdenum(IV) bonds and a site II Na^+ cation. The "zeolate" ligating properties of the monomeric *cis*-MoO_2 moiety (III, Figure 9) bears a strong resemblance to those of its redox active monomeric *fac*-MoO_3 partner (II, Figures 8 and 9), as shown in the aesthetically satisfying relationship between the redox interconvertible pair, illustrated in Figure 9.

Some Thoughts on $n\{MO_{3-x}\}$–$Na_{56}Y$. Some interesting and potentially useful features of the kind of "intrazeolite topotaxy" illustrated in Figures 6 and 7 include the following:

(i) The ability to produce zeolite-encapsulated "molecular metal oxides" under relatively mild conditions, in a clean and quantitative fashion.

(ii) The anchoring of "well-defined" monomeric, dimeric, and tetrameric oxometal units with "tuneable" oxidation states, to specific oxygen framework and extraframework cation sites.

(iii) Recognition of the concept of the "zeolate ligand", namely, a collection of interconnected four-ring and six-ring aluminosilicate units, structurally similar to macrocyclic crown ethers and which form a macrospheroidal multidentate multisite "rigid cavitate", with the ability to complex (stabilize, coordinate, cap, ligate) monomeric MO_3 and MO_2 moieties in much the same way as that found in

the coordination chemistry of known *fac*-trioxometal (LMO_3) and *cis*-dioxometal (LMO_2) materials.

(iv) From the coordination chemistry of *fac*-LMO_3 complexes of M = Mo, W, one learns that the propensity of "zeolate-ligated" MO_3 to form dimeric units in the case of M = W^{6+} and monomeric units in the case of M = Mo^{6+}, could be related to the anticipated greater intrinsic lability (reactivity) of the W^{6+} relative to the Mo^{6+} monomeric (ZO)···MO_3···(NaOZ) coordination sites.[5] In this way, one can satisfactorily rationalize the following: (a) the formation of (ZONa)···$O_2W(\mu\text{-}O)_2WO_2$···(NaOZ) from *trans*-(ZONa)···(OC)$W(CO)_4$(CO)···(NaOZ) yet (ZO)···MoO_3···(NaOZ) from *trans*-(ZONa)···(OC)$Mo(CO)_4$-(CO)···(NaOZ); (b) the thermal oxidation of (ZO)···WO_2-··(NaOZ) to (ZONa)···$O_2W(\mu\text{-}O)_2WO_2$···(NaOZ) yet (ZO)-··MoO_2···(NaOZ) to (ZO)···MoO_3···(NaOZ); (c) the formation of dimeric (ZONa)···$O_2W(\mu\text{-}O)WO_2$···(NaOZ) from dimeric (ZONa)···$O_2W(\mu\text{-}O)_2WO_2$···(NaOZ), yet the nonexistence of Mo^{5+}···Mo^{5+} analogues.

(v) Discovery of thermally interconvertible redox active "zeolate complexes" which can be considered to be the "molecular" metal oxide analogues of bulk MO_{3-x} nonstoichiometric Magneli crystallographic shear phases.[17]

(vi) Success in overcoming the usual difficulty in engineering "precisely defined" oxometal sites on various substrates (nanochemistry) of interest in catalytic, solid-state and materials chemistry; this suggests potentially valuable applications such as size- and shape-selective hydrocarbon oxidation and olefin metathesis catalysis, chemoselective oxygen/oxidation sensors, molecule-discriminating nanoelectronic and nonlinear optical devices (which could exploit the advantages of "quantum confinement" of metal oxide units which are semiconductors in their bulk form).

Topotactic Kinetics in Zeolate Nanoreaction Chambers

Kinetics and Mechanism. Very recently the first kinetic study for archetypical substitution reactions of PMe_3 and ^{13}CO with the well-defined intrazeolite system $n\{Mo(^{12}CO)_6\}$-$M_{56}Y$, where M = Li, Na, K, Rb, and Cs, was reported.[18] Excellent isosbestic points (mid-IR spectroscopy) and first-order dissociative behavior were obtained, the activation parameters indicating a highly ordered supramolecular transition state consisting of activated $Mo(^{12}CO)_6$ and PMe_3 or ^{13}CO, anchored to M^+ ions and/or oxygen-framework sites in the α-cage of the $M_{56}Y$ host lattice. Generally, an increase in reactant loading produced a decrease in the activating ability of the host lattice (negative cooperative effects), but for reaction with PMe_3, reactivity was enhanced at higher loadings, where it was believed that associative attack on $Mo(^{12}CO)_6$ by PMe_3 became important.

The global picture that emerged from this investigation was that the α-cages of zeolite Y behave as "zeolate" ligands toward extraframework charge-balancing cations to which organometallic and ligand guests can become attached. This kind of approach assists with the design of experiments and the understanding of cation and framework anchoring and guest loading effects on the activating parameters and reaction mechanisms occurring in zeolites compared to gas, solution, surface, and matrix phases where such data are available.

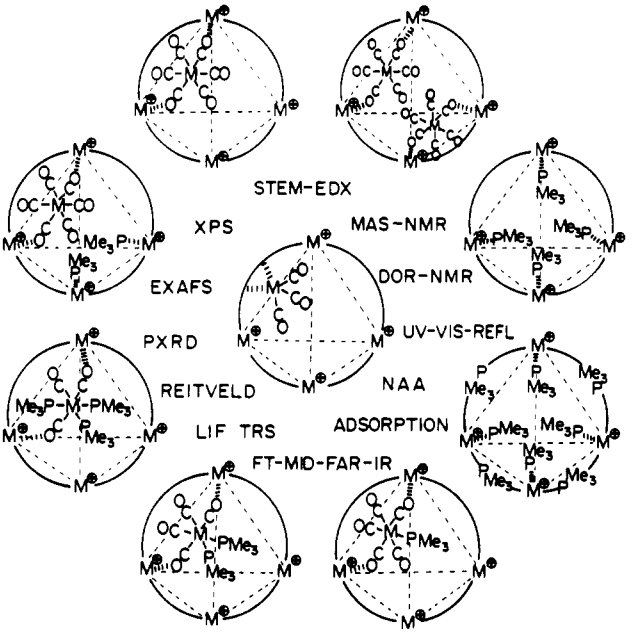

Figure 10. Multiprong approach to the characterization of the intrazeolite systems $n\{Mo(^{12}CO)_6\}$,$m\{L\}$-$M_{56}Y$, as well as relevant substitution products.[18]

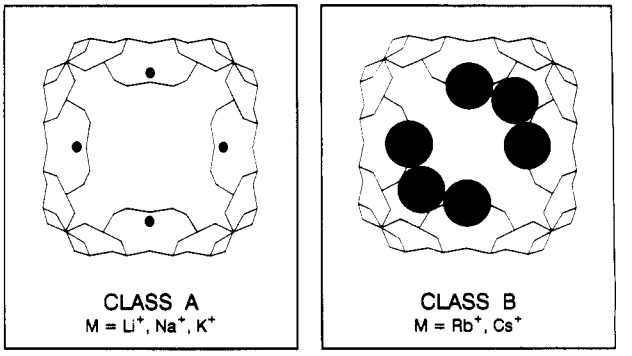

Figure 11. Illustration of class A zeolates (M = Li, Na, K) showing $4M_{II}$ cations and class B zeolates (M = Rb, Cs) with $4M_{II}$ and $2M_{II}$ cations. Two classes of reactivity in alkali-metal zeolates.[18]

In choosing an archetypical intrazeolite reaction for kinetic study, the following criteria should be ideally satisfied: (i) the intrazeolite reactants, possible intermediates, and products must be structurally and spectroscopically well-defined; (ii) as complete kinetic information as possible must exist for the same reaction in other phases; (iii) the reaction in all phases must be clean and simple. The thermal dissociative and associative substitution of ^{12}CO in $n\{Mo(^{12}CO)_6\}$,$m\{L\}$-$M_{56}Y$ by L = PMe_3 or ^{13}CO, where M = Li, Na, K, Rb, and Cs, nicely satisfies most of these criteria. A complete summary of pertinent knowledge acquired to date, obtained through a "multiprong approach" to the characterization of the $n\{Mo(^{12}CO)_6\}$,m-$\{L\}$-$M_{56}Y$ intrazeolite system, as well as relevant substitution products, is presented in Figure 10.

An important point concerns the four site II tetrahedrally organized M^+ cations (α-cage) which can trap reactants, intermediates and products in the arrangement sketched in Figure 10. For M = Rb and Cs, the extra two site III M^+ ions (α-cage) can provide additional Lewis acid centers for the anchoring and activation of occluded guest molecules. Recognition of this distinction between $M_{56}Y$, denoted class A, M = Li, Na, K, and class B, M = Rb, Cs (Figure 11), is central to the understanding of the two

(17) Adams, D. M. *Inorganic Solids*; Wiley: London, 1979.

(18) Ozin, G. A.; Özkar, S.; Pastore, H. O.; Poë, A. J.; Vichi, E. J. S. *J. Chem. Soc., Chem. Commun.* **1991**, 141. Ozin, G. A.; Özkar, S.; Pastore, H. O.; Poë, A. J.; Vichi, E. J. S. *Supramolecular Architecture in Two and Three Dimensions*; ACS Symposium Series, in press; *J. Am. Chem. Soc.*, in preparation.

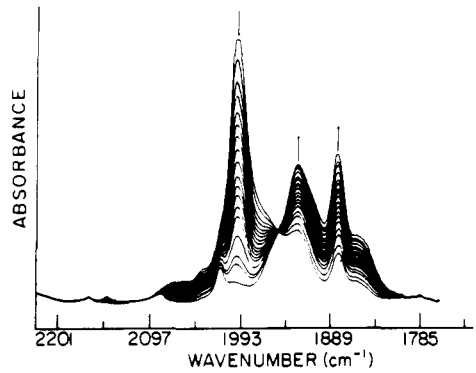

Figure 12. Mid-IR spectral traces of a kinetic run for 1.2{Mo-(^{12}CO)$_6$},24{PMe$_3$}–Na$_{56}$Y at 65.8 °C.[18]

Table III. Activation Parameters for Dissociative Reactions of Mo(^{12}CO)$_6$[18]

entering ligand	medium	$\Delta H^{\ddagger}$, kJ mol^{-1}	$\Delta S^{\ddagger}$, J K^{-1} mol^{-1}
none[a]	gas phase	157	38
^{14}CO	gas phase	126	−2
PBu$_3^n$	Decalin	133	28
^{13}CO[b]	Na$_{56}$Y	65	−127
PMe$_3$	Li$_{56}$Y	49	−182
	Na$_{56}$Y	70	−107
	K$_{56}$Y	88	−86
	Rb$_{56}$Y	75	−105
	Cs$_{56}$Y	57	−144

[a] Irreversible CO loss induced by pulsed laser pyrolysis technique at 670–760 K. [b] $P(^{13}CO)$ = 100 Torr.

different patterns of reactivity observed for ^{12}CO substitution of {Mo(^{12}CO)$_6$}–M$_{56}$Y by PMe$_3$ and ^{13}CO, briefly described below.

n{Mo(^{12}CO)$_6$}–Na$_{56}$Y ($n < 8$) undergoes ^{12}CO substitution reactions in the presence of PMe$_3$ in n{Mo(^{12}CO)$_6$}, m{PMe$_3$}–Na$_{56}$Y, or of ^{13}CO in n{Mo(^{12}CO)$_6$},m{^{13}CO}–Na$_{56}$Y to afford *cis*-{Mo(^{12}CO)$_4$(PMe$_3$)$_2$}–Na$_{56}$Y and fully labeled {Mo(^{13}CO)$_6$}–Na$_{56}$Y, respectively. No reaction intermediates were detected in the PMe$_3$ system, as suggested by the observation of an excellent isosbestic point (mid-IR monitoring, Figure 12). Noninvolvement of Mo(^{12}CO)$_5$PMe$_3$ under these conditions, as an intermediate in the formation of the *cis*-Mo(CO)$_4$(PMe$_3$)$_2$ product, was confirmed by direct impregnation of Mo(^{12}CO)$_5$PMe$_3$ in Na$_{56}$Y and the demonstration that this reacts much more slowly than Mo(^{12}CO)$_6$. Similar kinetic behavior was observed for reactions with PMe$_3$ in the entire series of hosts, M$_{56}$Y, and in all cases these reactions proceed by very well behaved first-order processes that involve what is believed to be a supramolecular assembly of Mo(^{12}CO)$_6$ precursor, PMe$_3$ ligands, and extraframework M$^+$ cations, all housed together in the supercage of M$_{56}$Y. Excellent Eyring plots yield the activation parameters $\Delta H^{\ddagger}$ and $\Delta S^{\ddagger}$ for each of the alkali-metal cations listed in Table III. A striking "volcano-shaped" effect is observed for these $\Delta H^{\ddagger}$ values on passing from Li$^+$ to Cs$^+$. This is counterbalanced by an "inverse-volcano" effect for $-T\Delta S^{\ddagger}$ (Figure 13).

The values for $\Delta H^{\ddagger}$ and $\Delta S^{\ddagger}$ are considerably smaller than those found for similar types of reactions in the solution and gas phases (Table III). This dramatic decrease, for what are described as "intracage" first-order dissociative ^{12}CO substitution reactions, is believed to originate in much stronger cation anchoring of the {Mo(^{12}CO)$_5$···(^{12}CO)}‡ transition state compared with that of the ground-state Mo(^{12}CO)$_6$. This could also account for the large negative values of $\Delta S^{\ddagger}$ since the much more weakly anchored Mo(^{12}CO)$_6$ in the ground state is transformed during ^{12}CO

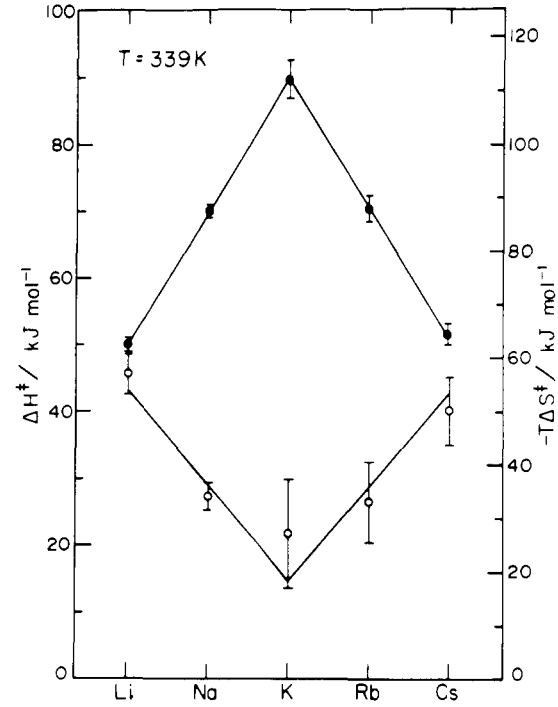

Figure 13. $\Delta H^{\ddagger}$ (●) and $-T\Delta S^{\ddagger}$ (○) for the reaction of n{Mo(^{12}CO)$_6$}, m{PMe$_3$}–M$_{56}$Y, where M = Li, Na, K, Rb, Cs.[18]

dissociation into the tightly anchored {Mo(^{12}CO)$_5$···(^{12}CO)}‡ transition state, this transformation being associated with increased back-bonding in the less highly coordinated intermediate, and the consequently greater negative charge on the oxygen atoms of the carbonyl ligands.

The volcano shape of the alkali-metal dependence of the $\Delta H^{\ddagger}$ parameter alerts one to the existence of the two classes of reactivity behavior for these dissociative substitutions in "alkali-metal cation–zeolate" environments, as alluded to earlier (Figure 11). The results indicate that the most strongly activated Mo(^{12}CO)$_6$ precursors have the most well organized {Mo(^{12}CO)$_5$···(^{12}CO)}‡ transition states (and vice versa). This kinetic behavior can be traced to differences that exist in the cation populations, topologies, spatial demands, and ionic potentials between the class A and class B zeolates (Figure 11). In essence the results imply that ionic potential control of the activation parameters dominates the chemical reactivity of Mo(^{12}CO)$_6$ in the $4M_{II}^+$ tetrahedral cation trap of class A materials, whereas both ionic potential and spatial demands of the more highly populated $4M_{II}^+ + 2M_{III}^+$ cation environment, found in class B materials, play the major role.

The above studies involved quite low loadings of Mo(^{12}CO)$_6$, with loadings of PMe$_3$ corresponding to the presence only of chemisorbed PMe$_3$, and loadings of ^{13}CO corresponding to a pressure of 100 Torr. The results can be understood in terms of the sequence of reactions depicted in Figure 14. The activation parameters for both PMe$_3$ and ^{13}CO intrazeolite substitution reactions are quite similar (Table III), indicating that the two processes have similar mechanisms. In both cases, the observed reaction rates are controlled by the dissociation of the first carbonyl from the "liberated" Mo(^{12}CO)$_6$ (Figure 14). During this loss of CO, the molybdenum moiety reattaches to the zeolite cage, which is followed by the loss of a second CO. The PMe$_3$ tethered to the other Na$^+$ cations then take the place of the missing CO group in the bound Mo(CO)$_4$ species. If, on the other hand, ^{13}CO ligands are present in the cage, they rapidly replace all of the ^{12}CO ligands in the bound Mo(^{12}CO)$_4$, and they fill the remaining vacant coordination sites to give Mo(^{13}CO)$_6$.

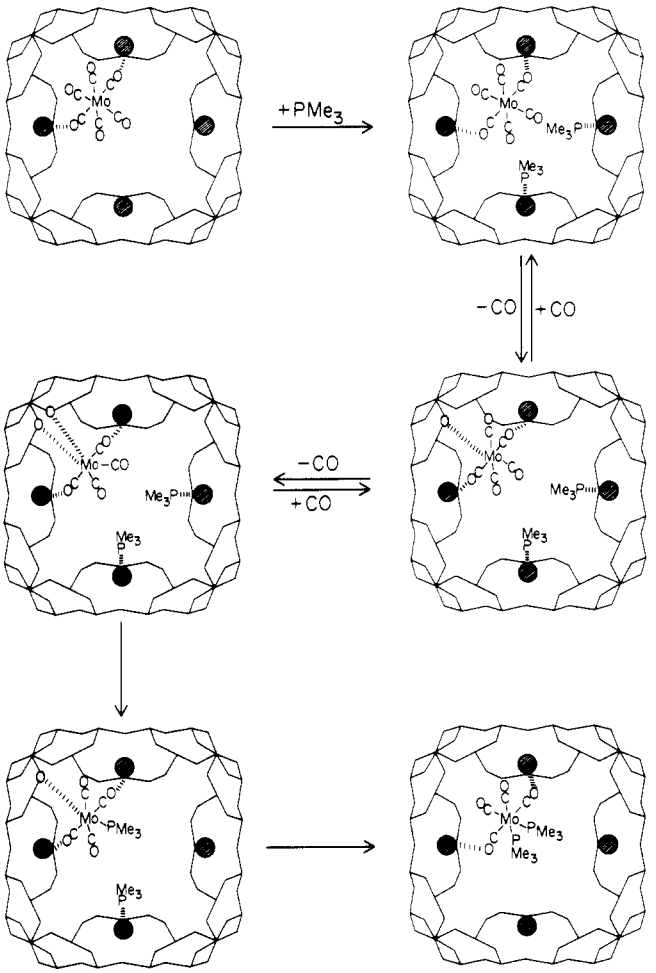

Figure 14. Basic mechanism for the dissociative substitution of ^{12}CO in $n\{Mo(^{12}CO)_6\}$–$Na_{56}Y$ by PMe_3.[18]

Because of page limitations, details of the $Mo(^{12}CO)_6$ and PMe_3 loading, as well as the ^{12}CO and ^{13}CO pressure dependence of the intrazeolite ^{12}CO substitution reactions of $\{Mo(^{12}CO)_6\}$–$M_{56}Y$ by PMe_3 and ^{13}CO, will not be presented here. The reader is referred to the original papers for this information.[18]

The Kinetic Product. The different reactivity patterns observed for ^{12}CO substitution of $\{Mo(^{12}CO)_6\}$–$M_{56}Y$ by PMe_3 in class A and class B zeolate nanoreaction chambers appears also to be reflected in the nature of the respective substitution product. Some of these have been characterized by a combination of mid-IR, ^{31}P-MAS NMR, and EXAFS structure analysis (Table IV).[19] In brief, for the $Na_{56}Y$ host at low loading levels of $Mo(^{12}CO)_6$ and PMe_3, the only reaction product was found to be $\{cis\text{-}Mo(CO)_4(PMe_3)_2\}$–$Na_{56}Y$ (Figure 15a). The $\{Mo(CO)_5PMe_3\}$–$Na_{56}Y$ product was observed only when the PMe_3 loading was considerably higher and when an external pressure of ^{12}CO was applied (Figure 15b). Under these circumstances it is believed that a bimolecular associative mechanism involving physisorbed PMe_3 can proceed at a sufficient rate to yield significant amounts of $\{Mo(CO)_5(PMe_3)\}$–$Na_{56}Y$.[18] In the $K_{56}Y$ system at low reactant loading, there was again no indication of reaction intermediates, and a unique reaction product, $\{fac\text{-}Mo(CO)_3(PMe_3)\}$–$K_{56}Y$, was observed (Figure 15c). In the case of PMe_3 substitution of $\{Mo(^{12}CO)_6\}$–$Rb_{56}Y$, the sole product was found to be the coordinately unsaturated $\{fac\text{-}Mo(CO)_3(PMe_3)\}$–$Rb_{56}Y$, its formation being attributed to the limited space, and diffusional constraints inside the α-cage when loaded with six large Rb^+ cations (Figure 15d).

One can conclude this kinetics section by stating that this investigation has yielded the first quantitative mea-

Table IV. EXAFS Structure Analysis Results for the Kinetic Products $\{Mo(^{12}CO)_x(PMe_3)_y\}$–$M_{56}Y$, Resulting from the Substitution of ^{12}CO in the Reactant Pair $n\{Mo(^{12}CO)_6\}$,$m\{PMe_3\}$–$M_{56}Y$ by PMe_3, Where M = Na, K, Rb[19]

sample[a]	bond length, Å	coordination no.	static disorder, Å²	inner potential, eV
$\{Mo(^{12}CO)_4(PMe_3)_2\}$–$Na_{56}Y$				
P(Mo)CO	2.57	1.59	−0.0016	1.4
P(Mo)*C*O	2.02	3.79	0.0000	−3.0
P(Mo)C*O*	3.16	3.79	−0.0014	−0.1
$\{Mo(^{12}CO)_3(PMe_3)_3\}$–$K_{56}Y$				
P(Mo)CO	2.58	3.07	0.0002	0.1
P(Mo)*C*O	2.01	3.19	−0.0034	−4.0
P(Mo)C*O*	3.16	3.19	−0.0019	−1.7
$\{Mo(^{12}CO)_3(PMe_3)_1\}$–$Rb_{56}Y$				
P(Mo)CO	2.55	1.27	−0.0045	−0.9
P(Mo)*C*O	1.97	3.63	0.0007	6.3
P(Mo)C*O*	3.14	3.63	−0.0026	−0.8

[a] Element-specific X-ray edge is indicated in parentheses; bond length and coordination number with respect to italicized element.

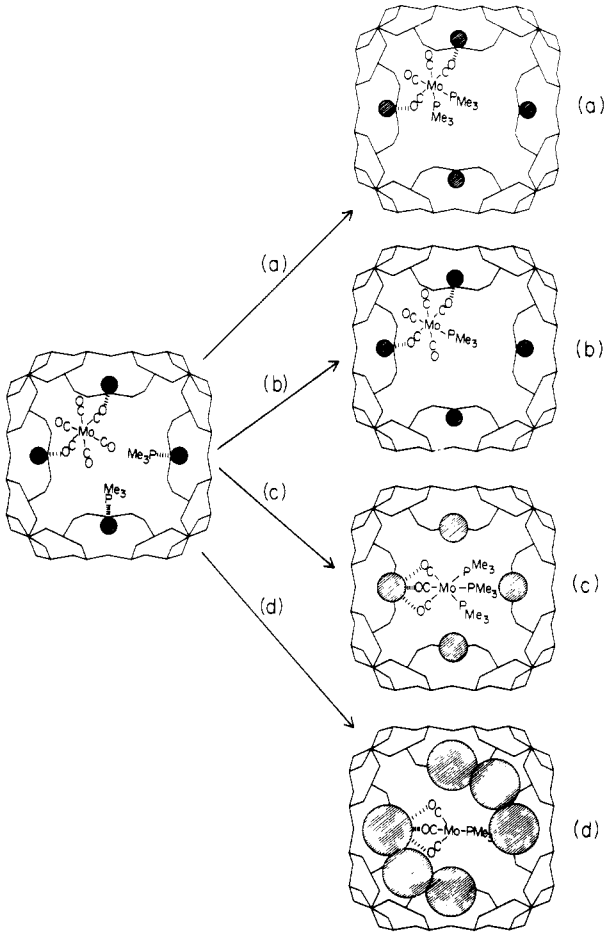

Figure 15. Cation control of the kinetic product in the reaction of $n\{Mo(^{12}CO)_6\}$–$M_{56}Y$ with PMe_3 for (a) Na, (b) Na with high loadings of PMe_3 or an external pressure of CO, (c) K, and (d) Rb.[19]

(19) Ozin, G. A.; Özkar, S.; Pastore, H. O.; Prokopowicz, R. *J. Phys. Chem.*, submitted.
Ozin, G. A.; Bowes, C. L.; Steele, M. R.; *Macromolecular Host–Guest Complexes*; M.R.S. Symp. Series, in press.

surements of the influence of the "internal perfect surface" of a zeolite host lattice on the chemical reactivity of encapsulated guests. The kinetics have unveiled an appealing picture of the α-cage nanoreaction chamber as a rigid macrospheroid multisite multidentate alkali metal–zeolate ligand. A model of this kind aids one with the design of experiments and the interpretation of cation and framework anchoring and guest loading effects on activation parameters and reaction mechanisms compared to gas, solution, surface, or matrix phases. Quantitative experiments of this kind are expected to be of great value in understanding intimate details of size and shape selective catalytic reactions, the origin of host–guest inclusion and molecular recognition phenomena, and the parameters that control a range of intrazeolite synthetic and self-assembly processes that are basic to the preparation of new solid-state nanoporous materials of interest in chemoselective sensing, quantum electronics, nonlinear optics, information storage and artificial photosynthesis, to name but a few.

Concluding Remarks: Zeolates

The global picture that emerges from our synthetic, structural, spectroscopic, and kinetic investigations is that the 13-Å nanoreaction chambers of zeolite Y behave as macrospheroidal multisite multidentate anionic ligands (zeolate or cavitate or spherate coordination) toward extraframework charge-balancing cations to which organometallic, metal oxide, and ligand guests can become attached. In this context an important point concerns the striking similarity between the oxygen framework four-ring and six-ring secondary building units found in zeolite Y and the macrocyclic polyether moieties found in 12-crown-4 and 18-crown-6, respectively (Figure 1). One notes the ability of these kinds of polydentate ligands to selectively coordinate and partially encapsulate alkali-metal cations. Lessons from the homogeneous and heterogeneous organometallic chemistry and catalysis literature as well as the field of zeolite science prepare one for the eventuality that Lewis acid cationic centres and Lewis base oxygen framework atoms of the above type are able to interact with the Lewis base and Lewis acid centers of organometallics, molecular metal oxides, and ligands (anchoring, coordinating, ligating, capping) to stabilize reactive moities, to cause distortions of structure, to provide changes in reactivity, and even alter the mechanism of a chemical transformation.

With the above in mind, the connection to the crown ether (cryptand and spherand) literature is enlightened, the relationship to the organometallic literature concerning the effects of alkali-metal anchoring and activating centers is recognized, and in particular the description of the nanoreaction chambers of zeolite Y as alkali-metal zeolate ligands can be appreciated.

Hopefully this zeolate coordination chemistry view of metal–ligand bonding in zeolite guest–host inclusion compounds will prove to be useful in the future development of the catalytic, solid-state chemistry, and materials science aspects of the field.

Acknowledgment. We are deeply indebted to the Natural Sciences and Engineering Research Council of Canada's Operating and Strategic Research Grants Programmes for generous financial support of this work. S.Ö. expresses his gratitude to the Chemistry Department, Middle East Technical University, Ankara, Turkey, for allowing him an extended leave of absence at the University of Toronto. Invaluable collaborations with as well as the generous exchange of ideas and information with members of the Zeolite/Molecular Sieve/Solid-State Chemistry community has made it a pleasure to work in this area. We particularly acknowledge the assistance of Drs. Edith Flanigen, Juan Garces, Thomas Bein, Karen Moller, Galen Stucky, and Alex Pines and Mr. Raz Jelinek as well as our colleagues in the Chemistry Department of the University of Toronto: Drs. Robert Morris, Peter Macdonald, and Anthony Poë. We also thank those members of the GAO group who have contributed directly to the development of the work described in this article: Drs. Richard Prokopowicz and Andrew Holmes, Mr. Alex Kuperman, and Ms. Heloise Pastore. We also acknowledge those members of the GAO group who have constantly been involved in helpful and stimulating discussions, Mr. Scott Kirkby, Mark Steele, Andrzej Malek, Ms. Susan Nadimi, and Mrs. Carol Bowes. The secretarial assistance of Ms. Helen Sarkissian continues to be of tremendous value.